ACTINIDE CHEMISTRY

Berkelium–carbon bonding in a tetravalent berkelocene

Dominic R. Russo[1,2]†, Alyssa N. Gaiser[1]†, Amy N. Price[1,2]†, Dumitru-Claudiu Sergentu[3,4]†, Jennifer N. Wacker[1], Nicholas Katzer[1,2], Appie A. Peterson[1], Jacob A. Branson[1,2], Xiaojuan Yu[5], Sheridon N. Kelly[1,2], Erik T. Ouellette[1,2], John Arnold[1,2], Jeffrey R. Long[1,2,6,7], Wayne W. Lukens Jr.[1], Simon J. Teat[8], Rebecca J. Abergel[1,2,9]*, Polly L. Arnold[1,2]*, Jochen Autschbach[5]*, Stefan G. Minasian[1]*

Interest in actinide–carbon bonds has persisted since actinide organometallics were first investigated for applications in isotope separation during the Manhattan Project. Transplutonium organometallics are rarely isolated and structurally characterized, likely owing to limited isotope inventories, a scarcity of suitable laboratory infrastructure, and intrinsic difficulties with the anaerobic conditions required. Herein, we report the discovery of an organometallic "berkelocene" complex prepared from 0.3 milligrams of berkelium-249. Single-crystal x-ray diffraction shows a tetravalent berkelium ion between two substituted cyclooctatetraene ligands, resulting in the formation of berkelium–carbon bonds. The coordination in berkelocene resembles that of uranocene, and calculations show that the berkelium 5f orbitals engage in covalent overlap with the δ-symmetry orbitals of the cyclooctatetraenide ligand π system. Charge transfer from the ligands is diminished relative to uranocene and other actinocenes, which maximizes contributions from the stable, half-filled $5f^7$ configuration of tetravalent berkelium.

Modern organometallic chemistry can be traced to the elucidation of a "sandwich" structure for ferrocene, $Fe(Cp)_2$ (Cp = C_5H_5), in the early 1950s by Wilkinson, Fischer, and colleagues (*1*, *2*). These reports nearly coincided with the discovery of two actinide elements, berkelium (Bk) and californium (Cf), which were reported by Seaborg and colleagues in 1950 (*3*, *4*). Despite this, for many years the fields of organometallic and actinide chemistry followed essentially separate trajectories. In contrast to $Fe(Cp)_2$, the first Cp complexes of actinides were highly reactive and air-sensitive (*5*), and actinide alkyl and carbonyl complexes—which are ubiquitous for d-block metals—were far too unstable to isolate (*6*). Interest in organoactinide chemistry was reignited with the synthesis and structural characterization of uranocene, $U(COT)_2$ (COT = C_8H_8), in the late 1960s by Streitwieser, Raymond and colleagues (*7*, *8*). $U(COT)_2$ had remarkable thermodynamic stability compared with actinide Cp complexes, which was attributed to the COT ligands being a better match for the U 5f orbitals in terms of size, energy, and symmetry (*9*). By 1976, all the actinocenes of the form $An(COT)_2$ (An = actinide), from Th through Pu (*10*–*12*), as well as the lanthanide analog with Ce, cerocene (*13*), were characterized. Save for some early microscale studies (*14*, *15*), the organometallic chemistry of transplutonium elements remained undeveloped until recently. The isolation and characterization of the trivalent Am and Cf complexes with Cp ligands, $Am(Cp^{tet})_3$ and $[Cf(Cp^{tet})_3Cl_2K(OEt_2)]_n$ (Cp^{tet} = C_5Me_4H), reported by Gaunt and colleagues in 2019 and 2021, respectively, constituted the first structural verifications of An–C bonds for elements beyond Pu (*16*, *17*). Ultraviolet–visible–near-infrared (UV-vis-NIR) spectroscopy and electronic structure calculations suggest that the bonding in these trivalent transplutonium organometallics is largely ionic in nature.

Several characteristics of $An(COT)_2$ complexes make them ideal subjects for spectroscopic and theoretical investigations of actinide covalency. Their high symmetry enables mixing of the 5f and 6d orbitals with the ligand frontier orbitals to form molecular orbitals of local σ, π, δ, and ϕ symmetry (*18*–*23*). The presence of an inversion center also restricts 5f- and 6d-orbital hybridization, which can complicate analyses of bonding. Further, the greater metal charge found in tetravalent actinocenes stabilizes the An 5f and 6d orbitals relative to trivalent actinide complexes, thereby reducing the difference in energy with ligand orbitals and enhancing covalent mixing (*21*). The discovery of a transplutonium COT actinocene would enable spectroscopic and theoretical studies across the actinide series and show how models of covalent bonding derived from the chemistry of early actinides can be applied to the transplutonium elements (*24*–*26*). However, the tetravalent oxidation state is difficult to stabilize for transplutonium elements and is particularly rare in molecular complexes that can be isolated and characterized by single-crystal x-ray diffraction (*27*). In targeting a transplutonium actinocene for synthesis, we noted that the tetravalent oxidation state is more accessible for Bk compared with the neighboring elements because of the stability of the associated half-filled $5f^7$ electronic configuration (*28*, *29*). In this study, we describe our efforts to develop the organometallic chemistry of tetravalent Bk, leading to the discovery of tetravalent Bk actinocene, or "berkelocene."

Synthesis

Developing high-valent Bk organometallic chemistry required overcoming several scientific and technical challenges because of the scarcity and high radioactivity of its most readily available isotope, ^{249}Bk [$t_{1/2}$ = 330(4) days]. Recent progress in molecular transuranium synthetic chemistry has provided the tools necessary to explore the synthetic chemistry of Bk (*25*, *26*). Synthetic protocols were developed that are compatible with the air and moisture sensitivity typical of organometallics and reproducible even at ultrasmall scales, while ensuring responsible stewardship of the precious and hazardous isotope. For example, the entire experimental process, from the first synthetic step through to isolation and characterization of the final product, was designed to be achievable within a ~48-hour time frame. Short-duration experiments were

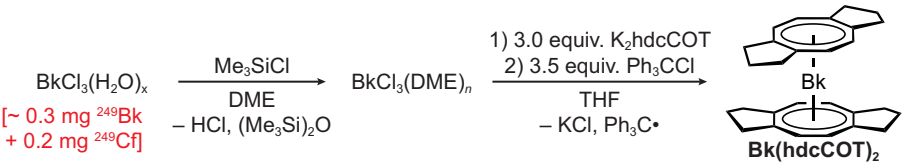

Fig. 1. Synthesis of a tetravalent Bk metallocene, $Bk(hdcCOT)_2$. The shorthand Ph_3C• refers to the radical by-product from reduction of Ph_3CCl, which couples to form Gomberg's dimer. Excess amounts of Me_3SiCl, $K_2hdcCOT$, and Ph_3CCl are used to ensure complete conversion to the $Bk(hdcCOT)_2$ product even in the presence of impurities due to the nature of small-scale synthesis (see SM, materials and methods).

[1]Chemical Sciences Division, Lawrence Berkeley National Laboratory, Berkeley, CA, USA. [2]Department of Chemistry, University of California, Berkeley, Berkeley, CA, USA. [3]Faculty of Chemistry, Alexandru Ioan Cuza University of Iași, Iași, Romania. [4]RA-03 (RECENT AIR) Laboratory, Alexandru Ioan Cuza University of Iași, Iași, Romania. [5]Department of Chemistry, University at Buffalo, Buffalo, NY, USA. [6]Department of Chemical and Biomolecular Engineering, University of California, Berkeley, Berkeley, CA, USA. [7]Department of Materials Science and Engineering, University of California, Berkeley, Berkeley, CA, USA. [8]Advanced Light Source, Lawrence Berkeley National Laboratory, Berkeley, CA, USA. [9]Department of Nuclear Engineering, University of California, Berkeley, Berkeley, CA, USA.
*Corresponding author. Email: rjabergel@lbl.gov (R.J.A.); pla@lbl.gov (P.L.A.); jochena@buffalo.edu (J.Au.); sgminasian@lbl.gov (S.G.M.)
†These authors contributed equally to this work.

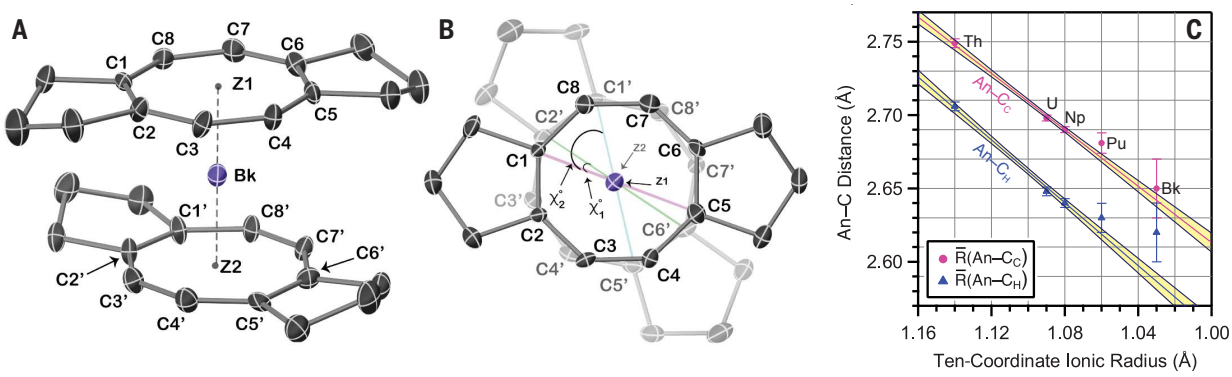

Fig. 2. X-ray crystallography. (**A**) Thermal ellipsoid (50%) plot of Bk(hdcCOT)$_2$, viewed from the side and (**B**) down the centroid–Bk–centroid axis. (**C**) Plot of the mean An–C distances (Å) in An(hdcCOT)$_2$ complexes (An = Th, U, Np, Pu, and Bk) as a function of the 10-coordinate ionic radius of the metal cations. Refer to the SM for details on the calculation of 10-coordinate ionic radii. Error bars are based on the standard deviation in the mean of chemically equivalent distances.

necessary to avoid potential product decomposition and crystal disintegration due to radiolysis and in-growth of ^{249}Cf, the primary daughter of ^{249}Bk. Additionally, the synthesis had to be resilient to ^{249}Cf impurities present in the starting material (~0.2 mg or ~0.8 μmol of Cf^{3+}), while also accommodating excess reagents left over from preceding synthetic steps. Crucially, no solvents or reagents could be used that would impede future Bk reprocessing or prevent proper disposal.

Synthetic protocols were designed for 0.5 mg (2 μmol of total metal content) scale reactions with all details of the procedure optimized in advance using Ce as a nonradioactive and abundant lanthanide surrogate to demonstrate reproducibility. Chemical oxidation (*28*) and electrolytic experiments have shown that the Bk^{4+}/Bk^{3+} reduction potential and its sensitivity to the surrounding ligand environment are comparable with those of Ce^{4+}/Ce^{3+} (*30*–*32*). In addition to unsubstituted COT, small-scale cerocene syntheses were tested using four substituted COT ligands with different solubilizing and electron-donating characteristics. The hdcCOT ligand (hdcCOT = hexahydrocyclopenta[8]annulene) consistently provided the Ce(hdcCOT)$_2$ complex when using ~0.5 mg of Ce, and hence hdcCOT was selected for subsequent Bk experiments [see supplementary materials (SM)] (*33*, *34*). Tetravalent cerocenes are best synthesized by oxidation of a trivalent cerium complex (*35*, *36*), so a variety of organic oxidants were also tested. Ultimately, chlorotriphenylmethane (Ph_3CCl) was selected as an oxidant owing to waste management constraints (see above). All other reaction conditions, including stirring times, solution concentrations, and the relative ratios of each reactant were optimized in advance during these small-scale preparations of Ce(hdcCOT)$_2$ (see SM).

The anhydrous precursor $BkCl_3(DME)_n$ (DME = 1,2-dimethoxyethane) was prepared as an off-white solid by treating a pale-green sample of hydrated $BkCl_3$ with Me_3SiCl in DME (Fig. 1) (*24*, *26*). After evaporation, the solid residue was suspended in tetrahydrofuran (THF) and 3 equiv of K_2hdcCOT were added to form a yellow-orange solution. No color change was observed after ~16 hours of stirring. Addition of a THF solution containing 3.5 equiv of Ph_3CCl resulted in an immediate color change to indigo. After work-up, evaporation of a *n*-pentane solution yielded indigo crystals that were analyzed by single crystal x-ray diffraction, confirming the formation of Bk(hdcCOT)$_2$.

Crystallography

The complex crystallizes in the space group $P\bar{1}$ with the Bk atom positioned on an inversion center and a hdcCOT$_{cent(1)}$–Bk(1)–hdcCOT$_{cent(2)}$ angle of 178.3(5)° (Fig. 2, A and B). The two hdcCOT rings are rotated about the Bk-centroid axis to form a pseudo-D_2 symmetric structure, with all four carbocyclic cyclopentane rings adopting a boat-like, all *endo* conformation (bending toward the Bk atom). The average torsion angle between the observed pseudo-D_2 conformation and a C_{2h} (eclipsed) conformation is 55(2)° (χ_2; Fig. 2B). By contrast, Ce(hdcCOT)$_2$ (see SM) crystallizes in the space group $P2_1/c$, exhibiting rigorous D_{2h} point symmetry, with the two carbocyclic cyclopentane rings adopting a chair-like, *exo-endo* conformation at low temperature. Notably, uranocene adopts a range of structural conformations depending on the nature of COT ligand substituents (*37*–*39*). For Bk(hdcCOT)$_2$, the potential energy associated with the staggered-to-eclipsed transformation for the *endo* system is computed to be nearly invariant between 0° to 30° (see below).

The C–C bond distances in Bk(hdcCOT)$_2$ are between 1.40(2) and 1.42(3) Å, which is typical of C–C distances in both substituted and unsubstituted COT ligands (*33*, *40*–*42*). The Bk–C distances range between 2.60(3) to 2.66(4), and the average Bk–hdcCOT$_{cent}$ distance is 1.88(2) Å. With additional structural data for other An(hdcCOT)$_2$ complexes (*43*), the crystal structure of Bk(hdcCOT)$_2$ provides a new opportunity to compare changes in ligand coordination across a large segment of the actinide series. Comparisons of bond distance require a precise definition of the metal's coordination number (*CN*), partially because ionic radii are dependent on *CN* (*44*). Although there are 16 carbon atoms coordinated to the metal centers in An(hdcCOT)$_2$ complexes, *CN* is defined here as equal to the formal number of electron pairs that are available for donation to the An metal from both hdcCOT ligands. Using nomenclature from the ionic model of electron counting, the cyclooctatetraene dianion is classified as an L_3X_2, five–electron pair donor ligand (three double bonds and two anionic carbon atoms) (*45*). Thus, a total of 10 electron pairs are involved in bonding for An(hdcCOT)$_2$ complexes, and therefore the An ions have a *CN* of 10.

Because the ionic radii for An ions with *CN* of 10 were not tabulated for all An, the ionic radii for *CN* of 10 were determined from the ionic radii for *CN* of 8, according to methodology described by Raymond and Eigenbrot (see SM) (*46*). Figure 2C compares changes in the An–C distances to the 10-coordinate ionic radii. The central C_8 ring of the hdcCOT ligand has two types of C atoms: those bonded to the carbocyclic rings (C_C) and those bonded to H atoms (C_H). Figure 2C shows that M–C_C distances are typically ~0.02 Å longer than M–C_H distances, which is attributed to differences in the steric environment. Linear fits provide good coefficients of determination (R^2) of 0.956 and 0.992 for the An–C_C and An–C_H data, respectively. Shorter An–C_C and An–C_H distances are observed for metals with smaller ionic radii. The strong linear correlation suggests that the bond metrics may be well rationalized, solely on the basis of changes in the metal ionic radii (*46*); however, differences in crystallographic disorder, local symmetry, space group, and crystal packing effects cannot be fully ruled out.

UV-vis-NIR absorption spectroscopy

Absorption spectra of Ce(hdcCOT)$_2$ and Bk(hdcCOT)$_2$ are provided in Fig. 3A. Intense

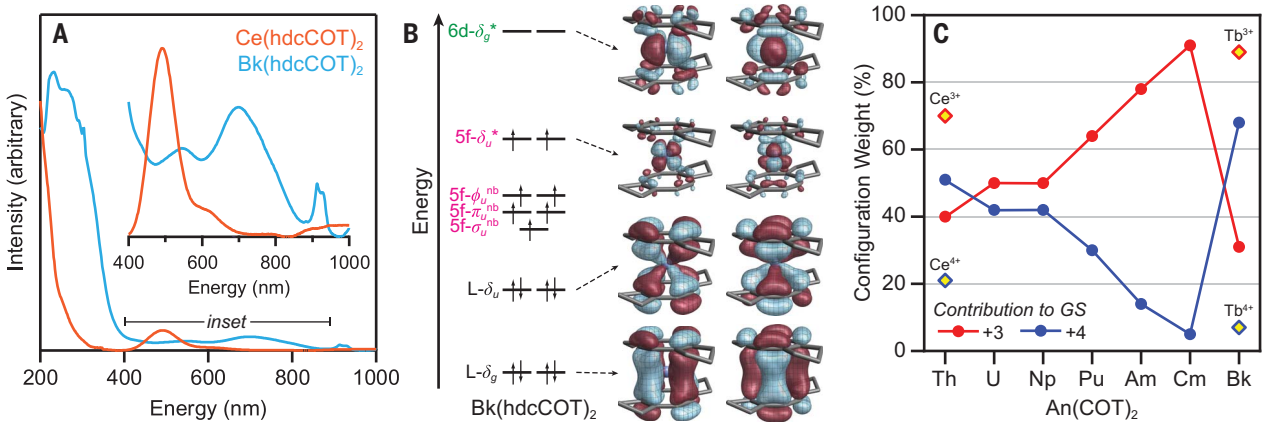

Fig. 3. Spectroscopic and theoretical analysis. (**A**) Experimental UV-vis-NIR absorption spectra of Bk(hdcCOT)$_2$ in *n*-pentane (blue) obtained from the mother liquor solution compared with a spectrum of Ce(hdcCOT)$_2$ in *n*-pentane (orange). The inset shows an expansion of the LMCT region. Experimental determination of extinction coefficients was precluded by the low sample concentration and by the presence of soluble redox byproducts (e.g., Gomberg's dimer and neutral hdcCOT). Absorption features >400 nm are partially attributed to Ph_3C• and Gomberg's dimer by-products formed during the oxidation with Ph_3CCl, which were not removed before the measurement (*57*). Sharp features at 913 and 927 nm are characteristic of f-f transitions, which could be associated with the $Bk^{4+}(5f^7)$ ion in Bk(hdcCOT)$_2$ or with small amounts of Bk^{3+} ($5f^8$) or Cf^{3+} ($5f^9$) impurities. (**B**) Qualitative valence molecular orbital diagram showing the most important metal–ligand bonding interactions and ordering of the nonbonding 5f orbitals from a CAS calculation targeting the ground state. (**C**) Contributions from An^{4+} and An^{3+} configurations to the ground state (GS) CAS wave functions of D_{8h}-An(COT)$_2$ (An = Th to Bk), expressed in an orbital basis with localized δ_u species. Data for Ce(COT)$_2$ and Tb(COT)$_2$ (*55, 56*) are provided for comparison.

features are observed in the visible region at 545 and 700 nm for Bk(hdcCOT)$_2$ and at 500 and 600 nm for Ce(hdcCOT)$_2$, which are commensurate with the purple-indigo colors observed for both compounds. As described in previous studies of Ce(COT)$_2$ (*35*, *47*), these bands are assigned to ligand-to-metal charge transfer (LMCT) transitions. Because the $4f^7$ configuration of Gd^{3+} is analogous to the $5f^7$ configuration of Bk^{4+}, we prepared [K(crypt)][Gd(hdcCOT)$_2$] as a reference for Bk(hdcCOT)$_2$ (see SM, materials and methods). The UV-vis spectrum of [K(crypt)][Gd(hdcCOT)$_2$] is essentially featureless in this energy regime with its first absorption band appearing at 345 nm. In this regard, the UV-vis spectrum [K(crypt)][Gd(hdcCOT)$_2$] closely resembles that of the ligand salt, K_2hdcCOT (fig. S10), which suggests that most transitions in this spectral region are ligand-based and not reflective of metal–ligand bonding. The slight increase in energy for the LMCT bands may reflect the higher energy of the Ce 4f orbitals relative to the Bk 5f orbitals, on the basis of fourth ionization potentials (*48*, *49*). Compared with other known Bk^{4+} compounds, the lower energy of the LMCT bands for Bk(hdcCOT)$_2$ relative to Bk[3,4,3-LI(1,2-HOPO)] (400 nm) (*50*) and Bk$(IO_3)_4$ (450 nm) (*26*) is attributed to the higher energy of the ligand-based C 2p versus O 2p atomic orbitals. Taken together with theory (see below), these observations and assignments are consistent with a Bk^{4+} organometallic complex.

Electronic structure calculations

Density functional theory (DFT) calculations (*51*) for isolated Bk(hdcCOT)$_2$ predict a global minimum structure with D_{2d} symmetry and a completely *endo* conformation of the carbocylic cyclopentanes. At higher energy, within 19 kJ mol^{-1}, are the *endo-exo* and *exo-exo* conformers (fig. S23). These structures have Bk–hdcCOT$_{cent}$ and average Bk–C$_{hdcCOT}$ distances of 1.88 and 2.61 to 2.65 Å, which are in excellent agreement with the experimental data (see above). The potential energy profile associated with the rotation between the calculated D_{2d} conformer and the experimentally observed D_{2h} geometry for the endo hdcCOT system is nearly flat between 0° and 30° (fig. S24), suggesting that the observed geometry of Bk(hdcCOT)$_2$ in the crystal could easily be due to crystal packing.

Relativistic complete active space (CAS) self-consistent field wave function calculations of all possible ligand-field spin states of the $5f^7$ configuration for the Bk^{4+} ion, followed by multireference treatment of the dynamic electron correlation and treatment of spin-orbit coupling (SOC), were performed for Bk(hdcCOT)$_2$ and the experimentally unknown Bk(COT)$_2$. The resulting energy-level scheme (fig. S25) shows an $^8S_{7/2}$ ground state, along with ligand-field-split Kramers components of $^6D_{7/2}$ ion parentage around 1.69 eV (corresponding to a photon wavelength of 733 nm). This energy, although somewhat overestimated, matches that of the sharp f-f transitions in the absorption spectrum at 913 and 927 nm (1.36 and 1.34 eV). Time-dependent DFT calculations of LMCT states (table S17) yield the most intense excitation around 500 nm [2.48 eV, Perdew–Burke–Ernzerhof (PBE) functional] and 450 nm (2.76 eV, PBE0), and assign it to a dipole-allowed, *z*-polarized L-$\delta_g \rightarrow$ f-δ_u* transition. The calculations therefore support the assignment of the experimental absorption feature at 545 nm (2.27 eV) when considering that previous calculations for M(COT)$_2$ also deviated from experimental UV-vis-NIR absorption energies by up to ~0.5 eV (*20*). LMCT states calculated near the observed band at 700 nm are assigned to L-$\delta_u \rightarrow$ f-δ_u* transitions, with small oscillator strengths because of the parity selection rule; the increased intensity observed experimentally for these transitions may arise from vibronic coupling, which was not accounted for in the calculations.

The CAS calculations were also used to evaluate the ground state configuration, chemical bonding, and the formal oxidation state for both D_{2d}-Bk(hdcCOT)$_2$ and the unsubstituted D_{8h}-Bk(COT)$_2$. When expressed in the basis of metal-ligand hybridized natural orbitals, the ground state for D_{2d}-Bk(hdcCOT)$_2$ and D_{8h}-Bk(COT)$_2$ is dominated by the $(L\text{-}\delta_g)^4(L\text{-}\delta_u)^4f^7d^0$ configuration. The wave function is essentially single-configurational (96% weight) when only the ground spin-octet state is targeted in the calculation. The ground state wave function was used in all subsequent analyses. However, it gradually becomes multiconfigurational when excited states are included in the state averaging. The $(L\text{-}\delta_g)^4(L\text{-}\delta_u)^4f^7d^0$ configuration has 87% weight in the ground state with a state average of 1 octet and 14 sextets, and 64% with a state average of 14 octet and 14 sextet states. Similarly to what previous spectroscopic and theoretical studies of bonding in early actinide sandwich complexes have found (*52*), metal–ligand covalency in D_{2d}-Bk(hdcCOT)$_2$ occurs primarily in the doubly degenerate L-δ_u and

L-δ_g orbitals (Fig. 3B), which have considerable metal weights (22% 5f and 26% 6d, respectively).

To evaluate the oxidation state, the ground state wave function can alternatively be expressed by using ligand- and metal-localized linear combinations of the bonding-antibonding δ_u/δ_u^* pairs, in which case the covalent ligand-to-5f donation appears primarily through admixture of charge-transfer configurations. Localization of the δ_u combinations on the metal and ligands, respectively, was achieved by "rotation" (in orbital space) between the bonding-antibonding pairs (22° angle). This results in 70% weight of the $5f^7$ (Bk^{4+}) configuration for D_{8h}-Bk(COT)$_2$ and D_{2d}-Bk(hdcCOT)$_2$ (Fig. 3C and fig. S26), indicating that both are meaningfully assigned as formally Bk^{4+} 3. Figure 3C presents the compositions of the ground state wave functions for D_{8h}-An(COT)$_2$ with An = Th–Bk when expressed in the aforementioned localized orbital sets, in terms of the metal oxidation state. Following common practice for f-element complexes, the assignment of the metal oxidation state is based on occupation of the f shell and disregards donation involving 6d, 7s, or 7p shells. From Th to Cm, in particular, there is a clear preference of the central metal for the trivalent oxidation state, especially beyond Np, which is in agreement with previous studies (*20*, *53*, *54*). A sharp decrease in weight of the +3 configuration occurs between Cm(COT)$_2$ (98%) and Bk(COT)$_2$ (33%), which is reflective of a decrease in net donation from the ligands into the 5f shell as both systems increase the relative weight of the stability and chemical inertness of the $5f^7$ configuration (*20*).

To understand how the stability of a half-filled $5f^7$ shell may lead to a greater weight of the Bk^{4+} configuration, Bk(hdcCOT)$_2$ was compared with its Ce and Tb analogs. Tb(COT)$_2$ has not been observed experimentally but was described in earlier theoretical work as having a ground state dominated by an 89% weight of the ionic $(L\text{-}\delta_g)^4(L\text{-}\delta_u)^3f^8d^0$ configuration, corresponding to Tb^{3+} (*55*, *56*). This can be attributed to the large fourth ionization energy of Tb, which is similar to that of Cm (*48*, *49*), such that the Tb^{4+} $4f^7$ configuration is comparatively high in energy and not sufficiently stabilized by COT^{2-} ligands. By contrast, the overlap between 5f and ligand orbitals that is evident in the natural orbitals for Bk(hdcCOT)$_2$ (Fig. 3B) must have a stabilizing effect on the Bk^{4+} ground state. A substantial degree of 4f-shell bonding is also apparent in the natural orbitals for Ce(hdcCOT)$_2$ and Ce(COT)$_2$; however, a large amount of charge transfer into formally empty 4f orbitals (in contrast to the partially filled 5f orbitals in the Bk case) means that these complexes have dominant Ce^{3+} character (Fig. 3C). The electron populations associated with the pairs of metal-COT–localized δ_u orbitals are $(L\text{-}\delta_u)^{3.67}(f\text{-}\delta_u)^{2.33}$ and $(L\text{-}\delta_u)^{3.15}(f\text{-}\delta_u)^{0.85}$ for Bk(hdcCOT)$_2$ and Ce(hdcCOT)$_2$, respectively. This suggests that the extent of ligand-to-metal donation is far more pronounced with Ce 4f-δ_u (0.85 electrons) than with Bk 5f-δ_u (0.33 electrons); that is, the berkelocene has a dominant 4+ character.

Conclusions

The discovery and structural characterization of Bk(hdcCOT)$_2$ shows that Bk^{4+}–C bonds can be stabilized in high-valent Bk organometallics and that organometallic complexes of rare and radioactive isotopes can be isolated and fully characterized starting from <0.5 mg of metal. The experimental data provide an opportunity to test electronic structure models across both the lanthanide and actinide series. The stark differences between Bk^{4+} and its lanthanide analogs are peculiar, given that Ce^{4+} and Bk^{4+} have similar reduction potentials and that Tb^{4+} and Bk^{4+} both have half-filled f shells. However, the half-filled Bk^{4+}-$5f^7$ configuration is stabilized by the productive metal–ligand overlap afforded by more radially extended 5f orbitals.

REFERENCES AND NOTES

1. G. Wilkinson, M. Rosenblum, M. C. Whiting, R. B. Woodward, *J. Am. Chem. Soc.* **74**, 2125–2126 (1952).
2. E. O. Fischer, W. Pfab, *Z. Naturforsch. B* **7** 377–379 (1952).
3. S. G. Thompson, A. Ghiorso, G. T. Seaborg, *Phys. Rev.* **80**, 781–789 (1950).
4. S. G. Thompson, K. Street, A. Ghiorso, G. T. Seaborg, *Phys. Rev.* **80**, 790–796 (1950).
5. L. T. Reynolds, G. Wilkinson, *J. Inorg. Nucl. Chem.* **2**, 246–253 (1956).
6. H. Gilman *et al*., *J. Am. Chem. Soc.* **78**, 2790–2792 (1956).
7. A. J. Streitwieser Jr., U. Mueller-Westerhoff, *J. Am. Chem. Soc.* **90**, 7364 (1968).
8. A. Zalkin, K. N. Raymond, *J. Am. Chem. Soc.* **91**, 5667–5668 (1969).
9. A. Streitwieser *et al*., *J. Am. Chem. Soc.* **95**, 8644–8649 (1973).
10. A. J. Streitwieser Jr., N. Yoshida, *J. Am. Chem. Soc.* **91**, 7528 (1969).
11. D. G. Karraker, J. A. Stone, E. R. J. Jones Jr., N. Edelstein, *J. Am. Chem. Soc.* **92**, 4841–4845 (1970).
12. D. F. Starks, T. C. Parsons, A. Streitwieser, N. Edelstein, *Inorg. Chem.* **13**, 1307–1308 (1974).
13. A. Greco, S. Cesca, W. Bertolini, *J. Organomet. Chem.* **113**, 321–330 (1976).
14. P. G. Laubereau, J. H. Burns, *Inorg. Chem.* **9**, 1091–1095 (1970).
15. P. G. Laubereau, J. H. Burns, *Inorg. Nucl. Chem. Lett.* **6**, 59–63 (1970).
16. C. A. P. Goodwin *et al*., *Angew. Chem. Int. Ed.* **58**, 11695–11699 (2019).
17. C. A. P. Goodwin *et al*., *Nature* **599**, 421–424 (2021).
18. J. G. Brennan, J. C. Green, C. M. Redfern, *J. Am. Chem. Soc.* **111**, 2373–2377 (1989).
19. M. Pepper, B. E. Bursten, *Chem. Rev.* **91**, 719–741 (1991).
20. A. Kerridge, N. Kaltsoyannis, *J. Phys. Chem. A* **113**, 8737–8745 (2009).
21. M. L. Neidig, D. L. Clark, R. L. Martin, *Coord. Chem. Rev.* **257**, 394–406 (2013).
22. S. G. Minasian *et al*., *Chem. Sci.* **5**, 351–359 (2014).
23. G. Ganguly, D.-C. Sergentu, J. Autschbach, *Chemistry* **26**, 1776–1788 (2020).
24. A. N. Gaiser *et al*., *Nat. Commun.* **12**, 7230 (2021).
25. S. S. Galley *et al*., *J. Am. Chem. Soc.* **141**, 2356–2366 (2019).
26. M. A. Silver *et al*., *J. Am. Chem. Soc.* **139**, 13361–13375 (2017).
27. M. N. Sokolova *et al*., *Inorg. Chem.* **48**, 9185–9190 (2009).
28. D. E. Hobart, J. R. Peterson, in *The Chemistry of the Actinide and Transactinide Elements*, vol. 3, L. Morss, N. Edelstein, J. Fuger, Eds. (Springer, 2006), chap. 10, pp. 1444–1498.
29. S. G. Thompson, B. B. Cunningham, G. T. Seaborg, *J. Am. Chem. Soc.* **72**, 2798–2801 (1950).
30. M. R. Antonio, C. W. Williams, L. Soderholm, *Radiochim. Acta* **90**, 851–856 (2002).
31. J. R. Stokely, R. D. Baybarz, J. R. Peterson, *J. Inorg. Nucl. Chem.* **34**, 392–393 (1972).
32. E. Wadsworth, F. R. Duke, C. A. Goetz, *Anal. Chem.* **29**, 1824–1825 (1957).
33. M. Hiller, M. Maier, H. Wadepohl, M. Enders, *Organometallics* **35**, 1916–1922 (2016).
34. J. D. Hilgar, A. K. Butts, J. D. Rinehart, *Phys. Chem. Chem. Phys.* **21**, 22302–22307 (2019).
35. A. Streitwieser, S. A. Kinsley, C. H. Jenson, J. T. Rigsbee, *Organometallics* **23**, 5169–5175 (2004).
36. U. Kilimann, R. Herbst-Irmer, D. Stalke, F. T. Edelmann, *Angew. Chem. Int. Ed.* **33**, 1618–1621 (1994).
37. K. O. Hodgson, K. N. Raymond, *Inorg. Chem.* **12**, 458–466 (1973).
38. A. Zalkin, D. H. Templeton, S. R. Berryhill, W. D. Luke, *Inorg. Chem.* **18**, 2287–2289 (1979).
39. A. Zalkin, D. H. Templeton, W. D. Luke, A. J. Streitwieser Jr., *Organometallics* **1**, 618–622 (1982).
40. A. Avdeef, K. N. Raymond, K. O. Hodgson, A. Zalkin, *Inorg. Chem.* **11**, 1083–1088 (1972).
41. D. J. A. De Ridder, J. Rebizant, C. Apostolidis, B. Kanellakopulos, E. Dornberger, *Acta Crystallogr. C* **52**, 597–600 (1996).
42. C. J. Windorff *et al*., *Inorg. Chem.* **59**, 13301–13314 (2020).
43. D. R. Russo *et al*., *Chem. Commun.* (2025).
44. L. Pauling, *The Nature of the Chemical Bond* (Cornell Univ. Press, 1960).
45. M. L. H. Green, G. Parkin, *J. Chem. Educ.* **91**, 807–816 (2014).
46. K. N. Raymond, C. W. J. Eigenbrot Jr., *Acc. Chem. Res.* **13**, 276–283 (1980).
47. F. Ferraro, C. A. Barboza, R. Arratia-Pérez, *J. Phys. Chem. A* **116**, 4170–4175 (2012).
48. X. Cao, M. Dolg, *J. Mol. Struct. THEOCHEM* **581**, 139–147 (2002).
49. X. Y. Cao, M. Dolg, *J. Mol. Struct. THEOCHEM* **673**, 203–209 (2004).
50. G. J.-P. Deblonde *et al*., *Nat. Chem.* **9**, 843–849 (2017).
51. D.-C. Sergentu, Raw output data for "Berkelium-Carbon Bonding in a Tetravalent Berkelocene", Version v1, Zenodo, (2024); https://doi.org/10.5281/zenodo.14032783.
52. A. H. H. Chang, R. M. Pitzer, *J. Am. Chem. Soc.* **111**, 2500–2507 (1989).
53. A. Kerridge, *Dalton Trans.* **42**, 16428–16436 (2013).
54. A. Kerridge, *RSC Adv.* **4**, 12078–12086 (2014).
55. W. J. Liu, M. Dolg, P. Fulde, *Inorg. Chem.* **37**, 1067–1072 (1998).
56. W. J. Liu, M. Dolg, P. Fulde, *J. Chem. Phys.* **107**, 3584–3591 (1997).
57. T. Nishiuchi *et al*., *Aggregate (Hoboken)* **2**, e126 (2021).

ACKNOWLEDGMENTS

Funding: This work was supported by the US Department of Energy (DOE), Office of Science, Office of Basic Energy Sciences, Heavy Element Chemistry Program at Lawrence Berkeley National Laboratory under contract DE-AC02-05CH11231. J.Au. acknowledges support for the theoretical component of this study from the DOE, Office of Science, Office of Basic Energy Sciences, Heavy Element Chemistry Program, under award DE-SC0001136. We thank the Center for Computational Research (CCR) of the University at Buffalo for providing computational resources. D.-C.S. acknowledges the computing infrastructure provided by the RECENT AIR grant agreement MySMIS 127324. J.A.B. and S.N.K. acknowledge support from a DOE Integrated University Program Fellowship at the University of California, Berkeley. This research used resources of the Advanced Light Source, which is a DOE Office of Science User Facility under contract DE-AC02-05CH11231. We acknowledge T. Albrecht for providing a fraction of a $^{249}BkCl_3$ stock initially supplied by the National Isotope Development Center, which is managed by the DOE Isotope Program. **Author contributions:** Conceptualization and writing – original draft: D.R.R., A.N.G., A.N.P., D.-C.S., R.J.A., P.L.A., J.Au., S.G.M.; Formal

analysis: D.R.R., A.N.G., A.N.P., D.-C.S., X.Y., S.N.K., E.T.O., S.J.T., J.Au., S.G.M.; Funding acquisition: J.Ar., J.R.L., W.W.L., R.J.A., P.L.A., J.Au., S.G.M.; Investigation: D.R.R., A.N.G., A.N.P., D.-C.S., J.N.W., N.K., A.A.P., J.A.B., X.Y., S.N.K., E.T.O.; Methodology: D.R.R., A.N.G., A.N.P., D.-C.S., J.W., N.K.; Project administration: D.R.R., A.N.G., J.N.W., W.W.L., R.J.A., P.L.A., J.Au., S.G.M.; Resources: W.W.L., S.J.T., R.J.A., P.L.A., J.Au., S.G.M.; Supervision: J.Ar., J.R.L., W.W.L., S.J.T., R.J.A., P.L.A., J.Au., S.G.M.; Validation: D.R.R., A.N.G., A.N.P., A.A.P., J.N.W., J.A.B., S.J.T.; Writing – reviewing & editing: all authors. **Competing interests:** The authors declare that they have no competing interests. **Data and materials availability:** Crystallographic data are available free of charge from the Cambridge Crystallographic Data Centre under CCDC 2365691, 2365692, 2365694, 2366024, and 2366039. Raw outputs from the calculations are deposited at Zenodo (*51*). All other data are available in the main text or the SM.

SUPPLEMENTARY MATERIALS

science.org/doi/10.1126/science.adr3346
Materials and Methods
Figs. S1 to S30
Tables S1 to S22
References (*58*–*112*)

Submitted 27 June 2024; accepted 23 January 2025
10.1126/science.adr3346